

# Chapter 1

## Motivation

# Chapter 2

## Ion Trap Apparatus

A vast effort is spent on the initial build-up of the an ion trap system, but throughout the life of the experiment, a greater effort is spent on its daily maintenance. I hope that this chapter will serve as a resource for future members of the FastGates team, as well as provide a useful recipe for anyone building a similar system.

Due to the size and complexity of the system, we introduce an initial overview of the design, motivated by the desired functions. As the name suggests, an ion trap experiment aims to confine arrays of single ions, this is achieved by static and dynamic electric fields which, due to the ions possessing non-zero electric charge, can provide trapping potentials, section 2.2. Due to the fragility of the internal states of the ion (these are state of the art sensors after all), we must take great care in isolating the ion from any noisy environment. This neccesitates the use of ultra-high vacuum (UHV) systems, section 2.3, vibration isolation, and magnetic shielding, section ???. To manipulate the internal electronic states of the ion, we create local electric and magnetic fields using RF antennae and, in this work, lasers, sections 2.4 and 2.4.1. Finally, to interface with the apparatus we have built, at the time scales set by our interaction strengths, we require a sophisticated and custom control system which is discussed in section ??.

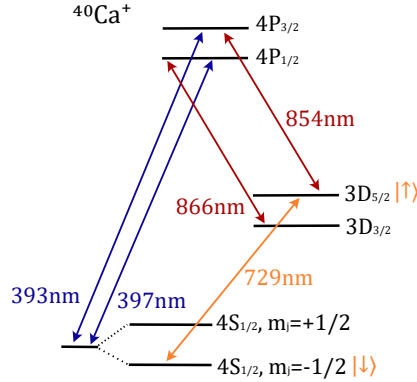


Figure 2.1: Electronic energy levels of  $^{40}\text{Ca}^+$ , which will be used in this thesis. The levels are split by the Zeeman effect due to a 5 G external magnetic field (they are shown explicitly only for the ground state). The transitions marked are required for cooling and control over the ion. We shall use the optical-qubit with a quadrupole transition at 729-nm. XXX TODO: Add zeeman levels for  $D_{5/2}$ .

## 2.1 System Design

## 2.2 The Ion Trap

To create trapping potentials we use linear Paul traps, a schematic of such is shown in Figure 2.2 (a). As explained by Earnshaw’s theorem, ( $\nabla^2 V = 0$ ), a stable stationary point in 3D can not be realized using only static electric potentials,  $V$ , as if the potential is confining in two dimensions, it will be anticonfining in the third. Therefore, to achieve stable trapping either an oscillating electric field (Paul trap [?]), or a static magnetic field (Penning traps [?]) must be utilized to create a confining pseudopotential.

Recently, the microfabricated surface style linear Paul trap has gained popularity due to the maturity of chip fabrication technologies [?] and the potential route to scalability this offers. In the surface trap, the 3D radial and axial electrodes of a “macro” trap are effectively projected onto a 2D surface. The stable point of such a trap is typically on the order of 50  $\mu\text{m}$  from the chip surface. The ease of fabrication of surface traps has allowed the creation of complex multizone devices with many DC electrodes. These mul-

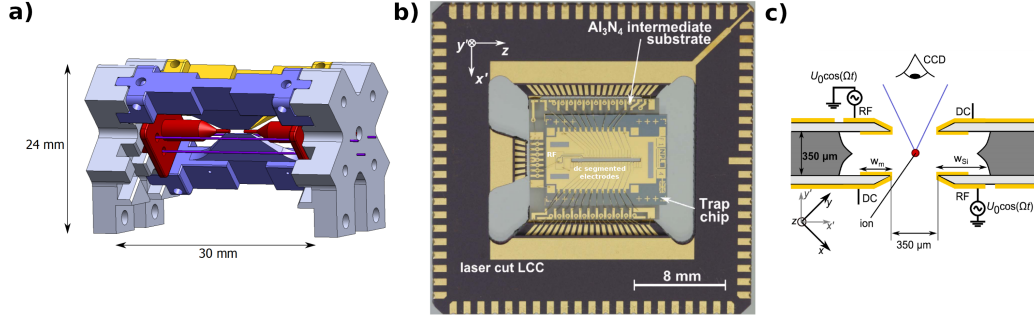


Figure 2.2: **a)** XX Place holder figure. **b)** The NPL trap in use in this thesis. This is a microfabricated, segmented, multilayer trap. **c)** A cross sectional view of the NPL trap showing the RF and DC electrode positions. Figures from [?].

tizone traps enable the shuttling of ions, a requirement for Quantum CCD type architectures [?]. However, this surface style geometry typically come with two costs: the depth of the trapping potential is often greatly reduced, and the close proximity of the surface to the ion can be a large contributor to motional heating rates [?].

The *NPL* microfabricated 3D trap [?, ?], as is used in our experiment, brings together the advantages of chip fabrication as well as the low heating rates and high trapping depths of a 3D style trap with greater ion-surface distances. This is achieved by a multilayer chip as shown in Figure 2.2 (b, c). The radial trapping is provided by RF rails on opposite diagonals of the slit whilst axial trapping may be realized by the numerous DC electrodes. The ion-surface distance is now of the order  $250 \mu\text{m}$  and we have demonstrated heating rates of  $33(3) \text{ q/s}$  on a 4 MHz radial mode (see section 3.3.2).

We aim for an axial ion separation of around  $5 \mu\text{m}$  which, for  $^{40}\text{Ca}^+$  ions means a trapping potential of  $\omega_z \approx 2\pi \cdot 1.6 \text{ MHz}$ . This ion separation was chosen to reduce the cross talk between ions when singly addressed (see section 2.4.2).

We are targeting approximately 5 MHz for our radial frequencies, as we shall use radial addressing for two-qubit entangling gates. The choice of this higher frequency is motivated by several factors. The Doppler cooling limit ( $\bar{n} = \Gamma/\omega$ , where  $\Gamma$  is the transition linewidth and  $\omega$  is the frequency of the cooled mode) inversely scales with the mode frequency. Consequently,

higher mode frequencies result in lower temperatures following initial cooling. Additionally, a higher center-of-mass radial mode enables greater frequency separation of radial modes in a multi-ion crystal, which allow for greater selectivity of participating modes.

Using the pseudopotential approximation [?] for the confining field, we can find a trapping frequency in one radial direction  $\omega_p$

$$\omega_p = \frac{e\alpha V_{RF}}{\sqrt{2}\Omega_{RF}M\rho^2}, \quad (2.1)$$

where  $\alpha$  is a factor of order unity given by the geometry of the trap,  $V_{RF}$  and  $\Omega_{RF}$  are the voltage and frequency provided to the RF-electrode,  $M$  is the mass of the ion, and  $\rho$  is the ion-RF electrode separation. Applying some DC voltage on the axial electrodes leads to axial confinement with frequency  $\omega_{ax}$ , but must defocus the radial confinements as the total curvature of the pseudopotential must remain constant,

$$\omega_{rad} = \sqrt{\omega_p^2 - \omega_{ax}^2/2}. \quad (2.2)$$

Due to the geometry of the DC electrodes with respect to the ion chain, the *NPL* trap focuses one of the radial modes and defocuses the other when the DC electrodes are increased,

$$\omega_{rad\pm} = \sqrt{\omega_p^2 - (1 \mp \beta)\omega_{ax}^2/2}, \quad (2.3)$$

where  $\beta$  is some factor due to the geometry of this geometry. From simulation  $\beta > 1$  for  $\Omega_{RF} = 2\pi \cdot 23$  MHz and  $V_{RF} = 200$  V and so one radial mode increases with DC voltage applied and one decreases.

	$V_{RF}/V$	$V_{DC}/V$	$\Omega_{RF}/(2\pi \cdot \text{MHz})$	$\omega/(2\pi \cdot \text{MHz})$		q
				$\omega_{ax}$	$\omega_{rad}$	
Experiment	200	-7	23	1.6	4.9	0.61
Loading	100	-2	23	0.8	2.0	0.25

Table 2.1: Simulated trapping parameters for both “Experiment” and “Loading” settings  $^{40}\text{Ca}^+$  with the *NPL* trap. The “Experiment” setting is optimized for high axial mode frequencies whilst the “Loading” setting maintains a lower q factor for practical loading.

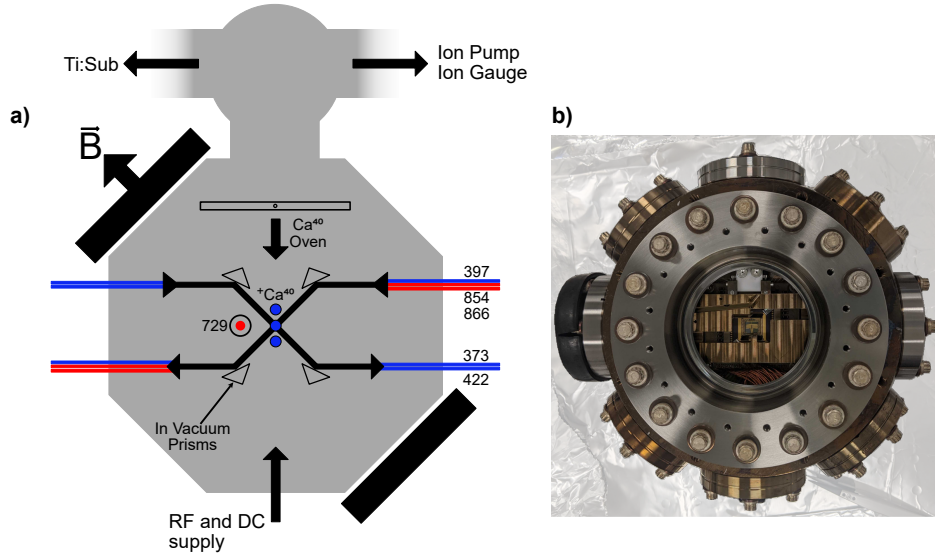


Figure 2.3: **a)** XXX Placeholder figure. A schematic of the vacuum chamber. Wavelengths apart from 729-nm enter through the side CF40 viewports and are directed onto the ions by in vacuum prisms. The 729-nm light enters through the larger CF100 viewports. **b)** A photograph of the assembled system prior to baking.

A possible set of parameters to achieve  $\omega_{ax} = 2\pi \cdot 1.6$  MHz and  $\omega_{rad+} = 2\pi \cdot 4.9$  MHz can be seen in the “Experiment” trapping in Table 2.1.

From the Mathieu equations, the areas of stability depend upon a factor  $q$  [?], where  $q = 2\sqrt{(2)}\omega/\Omega_{RF}$ . Generally, we require  $q$  to be as low ( $q < 0.3$ ) for convenient trapping. To satisfy this requirement a “Loading” setting (with parameters in table 2.1) may be used with  $q = 0.25$  and then the  $V_{RF}$  ramped to the “Experiment” trapping for high radial mode frequencies.

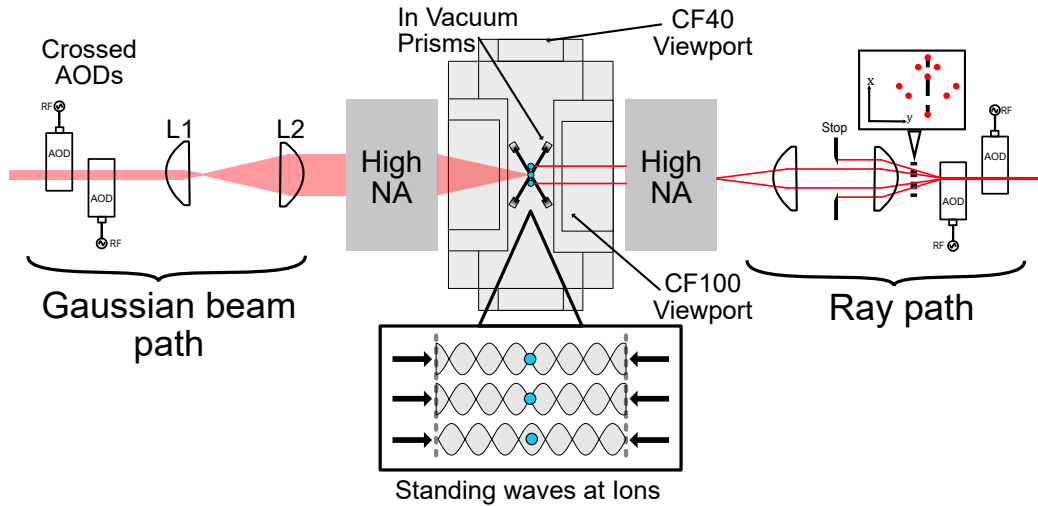


Figure 2.4: XXX Placeholder figure. The standing wave single addressing system. Dual high NA objectives focus the light to a tight waist at the ions location. AODs are used to steer the light to only selected ions. The left hand side of the figure shows the Gaussian profile of the light, whilst the right hand side shows a ray representation of how two singly addressing spots are formed at the ions. L1 is a telecentric scanning lens and in combination with L2 form a beam expander.

### 2.2.1 Trap RF Chain

### 2.2.2 Trap DC Voltages

## 2.3 Beam Geometries and Vacuum System

### 2.3.1 Vacuum System

### 2.3.2 Optical Access

## 2.4 $\text{Ca}^+$ Laser Systems

### 2.4.1 Narrow Line Width 729 Laser

Lasers are a key tool for creating the highly localised, strong electric field amplitudes and gradients needed to drive both carrier and sideband transi-

tions of the trapped ion.

As shown in Figure 2.1, we will use two levels within the  $4S_{1/2}$  to  $3D_{5/2}$  manifolds to define our qubit. This is an electric quadrupole transition as  $\Delta l = 2$ . For the Calcium ion this transition is at 729-nm, and so we use a near resonance 729-nm laser to implement single- and multi-qubit gates (sections 3.2.4 and 3.5). We also use this transition, after Doppler cooling, for resolved sideband cooling to bring the motional mode close to its ground state (as discussed in section 3.3.1).

This transition is narrow line width due to the long lived  $3D_{5/2}$  state, and so, for power efficiency, we must use a narrow linewidth laser. For our “fast entangling gates” use case we require large electric-field intensities at the ion to drive sideband transitions, this will be discussed further in the single-addressing and two-qubit gate sections, but here it is sufficient to say we require  $\sim 100$  mW of light at the ion plane. Here we describe the built system consisting of a Ti:Saph laser system pumped with by an Nd:YAG 532-nm laser.

We pump an *M2 Solstis* Ti:Saph [?] with 18 W of 532-nm light from a *Coherent Verdi-V* system [?] to produce around 5W of 729-nm light. The Ti:Saph is engineered to operate with a stable  $< 50$  kHz linewidth. Ti:Saph crystals have broadband gain profiles [?], which is often exploited in research environments to create frequency tunable laser systems. We however want a narrow linewidth, single frequency laser, and so the *Solstis* has multiple intracavity frequency selective elements. These consist of (in order of coarse frequency selectivity), a birefringent filter, a tunable Fabry-Pérot etalon, and the surrounding bow-tie cavity. For stable single mode operation, the *Solstis* employs an active “dither” servo to lock the peak of etalon transmission to one of the cavity longitudinal mode. This dither consists of periodically varying the etalon spacing with a frequency of around 20 kHz. We must be aware of this dither frequency as the phase modulation leads to the creation of sidebands on our light which can interact with the ion causing unexpected errors in gates. We can observe this dither frequency (and harmonics of it) with our ion via composite pulse experiments, however it is currently not expected to be a limiting source of error in any of our desired interactions we study.

As mentioned, the *Solstis* alone can operate with linewidths of  $< 50$  kHz, however we push this further by referencing the Ti:Saph output with an ultra high finesse cavity by *Stable Laser Systems* and applying a Pound-Drever-



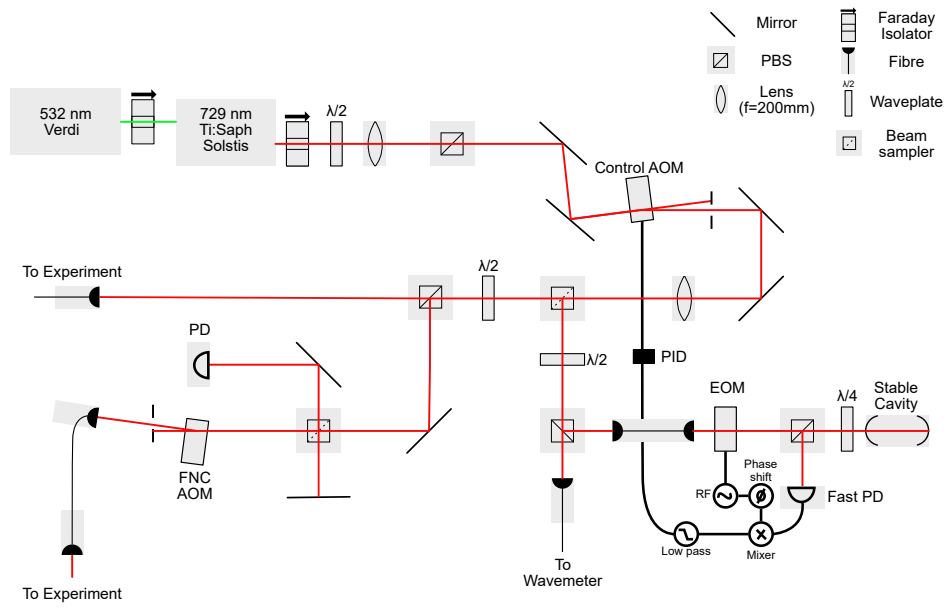


Figure 2.5: The 729-nm system. A Ti:Saph laser tuned to 729-nm is pumped by a 532-nm source. Light is picked off at the first beam sampler to stabilise by PDH locking to a cavity.

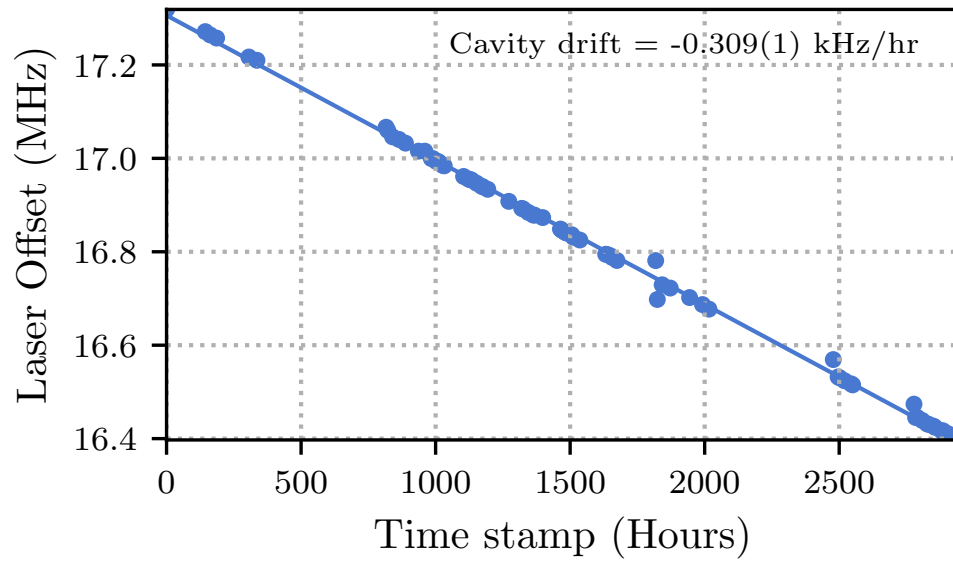


Figure 2.6: Cavity drift over 125 days. Extracted by reference to ion transition.

Hall (PDH) lock [?]. A schematic of our 729-nm system is shown in Figure 2.5. PDH locking requires applying two sidebands via an electro-optical modulator (EOM) to the light and directing it onto the stable cavity. The light reflected from the cavity is then directed onto a fast photodetector (*Thorlabs PDA10A2*). The reflection from the cavity consists of the interference between the carrier and the sidebands which have been respectively altered by the cavity transfer function. The photodetector signal is mixed down with the same oscillator signal as provided to the EOM but delayed by some chosen phase, and finally low pass filtered to produce a signal for use as the error signal in the servo loop. This error gives a measure for how far the carrier frequency is from the stable cavity resonant frequency and is used for feedback onto the control AOM situated after the Solstis. The electronics for this control loop are provided also by Stable Laser Systems in the form of their *FPGA Servo* lock box. For an effective PDH lock, we require both short and long term stability of our reference cavity. To ensure the cavity is insensitive to the environment, it is made of an ultra low expansion material. We temperature stabilise the cavity at the zero crossing temperature of 30.6°C, and it is further isolated by being stored in a vacuum system at  $< 1e - 7$  mbar. We measure a long term cavity drift of 309(1) Hz/hr over 125 days, seen in figure 2.5. This measurement uses the ion as a frequency reference to probe the cavity frequency and is discussed in section 4.1.2.

Figure 2.5 displays the other beam paths for our 729-nm system. Some light is picked off and sent to a wavemeter to continuously monitor the frequency. However, the majority is coupled to two output fibres for our experiment and another within the group. We transport the 729-nm light from a dedicated laser lab to a room containing the trap apparatus by a 10 m single mode polarization maintaining fibre (*SKXXX*). The fibre is beneficial in cleaning up the mode from the Ti:Saph, however it can introduce phase noise due to mechanical and thermal effects along the 10 m length. To remove this introduced noise we utilise passive stabilisation in the form of thick foam tubing along the fibre length as well as active stabilisation by popular fibre-noise-cancellation technique [?]. This topic has been discussed extensively in multiple PhD and Masters theses [?], and so here we only quote the relevant control aspects of our arrangement. We use the *Sinara Stabilizer* [?] board, a dual channel PID microcontroller, with the *Pounder* [?] mezzanine board, a dual channel PDH lock generator. The FNC PID software was developed by Ayush Agrawal [?]. A comparison of spin coherence times is shown in section 3.2.2 with and without fibre noise cancellation enabled.

### 2.4.2 Single Addressing System

## Chapter 3

# Experiment Characterisation

Before we can dive into running novel experiments involving the motion and spin of the atoms, we need to characterise our apparatus. This allows us to both benchmark our system against state of the art results, and to reveal any current limitations of the apparatus which we may need to address.

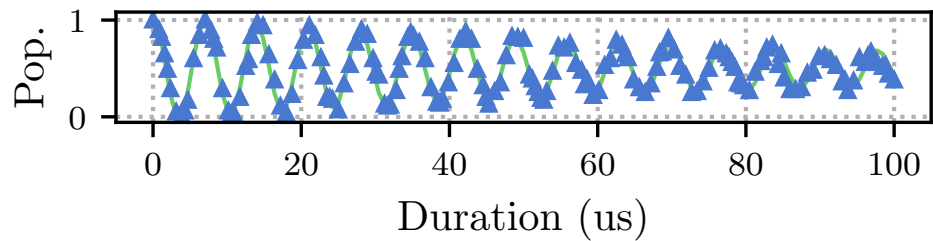


Figure 3.1: Long duration Rabi Flop with fitted decaying flop.

## 3.1 Quadrupole Transitions

## 3.2 Spin

### 3.2.1 Rabi and Ramsey Scans

Here we briefly describe the method in which we extract Rabi frequencies and single qubit gate durations. Long Rabi flop (100 us), fit out carrier frequency of  $2\pi \times 0.0716(1)$  MHz and Decay rate of  $0.0107(7)$  1 / us. See long flop. This is 1 mW of power on m1\_m3 transition before we changed polarization. Fit with decaying cos function

$$\frac{1 + e^{-\lambda t} \cos(2\Omega t)}{2}, \quad (3.1)$$

### 3.2.2 Spin Coherence Times

Individual gate fidelities are ultimately limited by loss of coherences of the two qubit states due to either dephasing or by the natural lifetime of the upper level. By our choice of ion and qubit levels, defined between the ground  $4S_{1/2}$  state and the metastable  $3D_{5/2}$  state, we can expect a lifetime limited coherence time of  $\tau = 1.1$  s [?]. In practise, mainly due to imperfect tracking of laser frequency and magnetic field drifts (as mentioned above), we see coherence times dominated by dephasing. To discern between these two noise sources, we may exploit the fact that we have multiple Zeeman levels within our  $3D_{5/2}$  state with varying magnetic field sensitivities. We also have the ability to define our qubit on the Zeeman split ground state, which decouples dephasing due to the laser from measured coherence times. We perform Ramsey scans with varying mid-sequence delay durations to extract the coherence times, an example of which can be seen in figure ???. In characterising the spin coherence times, we hope to explore both the efficacy of the magnetic shielding surrounding the ion trap, as well as the stability of the 729 nm laser.

Figure ?? shows how the magnetic shielding effect coherence times of three transitions, XX, YY and ZZ, with magnetic field sensitivities of XX, YY and ZZ respectively. From this we find that without the shielding, we are strongly limited by external magnetic field noise, and with full sheilding we suppress this noise to where we are dominated by laser phase noise. To find the factor by which the magnetic field noise is attenuated, we can compare

the coherence times of the laser phase insensitive transition with and without the box. We find an attenuation factor of XX, which is XXconsistent with the expected attenuation factor of the mu-metal shielding.

With the shielding in place, we compare the coherence times of the  $4S_{1/2}, m_j = -1/2 \leftrightarrow 3D_{5/2}, m_j = -5/2$  with fibre noise cancellation (see section 2.4.1) and without, figure ???. We find that the coherence time is improved by a factor of XX, with FNC enabled. Our current spin coherence time of XX ms is limited by the laser phase noise, and we expect to be able to push this to [ref R. Oswald] by improving the laser PDH stability. However, for the immediate planned experiments (see section ???), these improvements will be a low priority due to other likely dominating error sources in the motion of our ions.

### 3.2.3 State Preparation and Measurement

To utilise two levels of the ion as a qubit, we need to be able to selectively prepare the ion into one of the Zeeman levels of the ground state. As mentioned in section ??, we are operating at a low magnetic field of 5 G, leading to a splitting between the Zeeman levels of less than 21 MHz, the natural linewidth of the 397 nm transition. This means we cannot optically pump using 397 nm frequency selectivity. Further, due to the constraint of beam geometry from the in vacuum optics, we can not use polarisation selectivity of the 397 nm transition. Instead, we use the narrow line width 729 nm laser on resonance with the  $4S_{1/2}, m_j = +1/2 \leftrightarrow 3D_{5/2}, m_j = -3/2$  transition, and the 854 nm deshelling laser on resonance, to optically pump into the  $m_j = -1/2$  Zeeman level we define as our qubit ground state.

To measure the qubit state of the ion, we apply the 397 nm and 866 nm lasers and count 397 nm photons scattered. From the level diagram shown in figure ??, we can see that upon turning on the 397 nm laser, if we are in  $|0\rangle$ , photons will be scattered, and if we are in  $|1\rangle$ , then no photons will be scattered. To optimise the fidelity of measurement we ensure that the signal is discernible with low error from any background counts on the camera. In general, improving the number of signal counts can be achieved by tuning the 397 nm laser near to the transition resonance, by increasing the readout duration, or by increasing the percentage of scattered photons captured by the imaging system. Practically we desire that the readout step does not heat the motion of the ion and so we red detune the 397 nm laser to a similar setting as for Doppler cooling (see section 3.3.1). The parameters we use

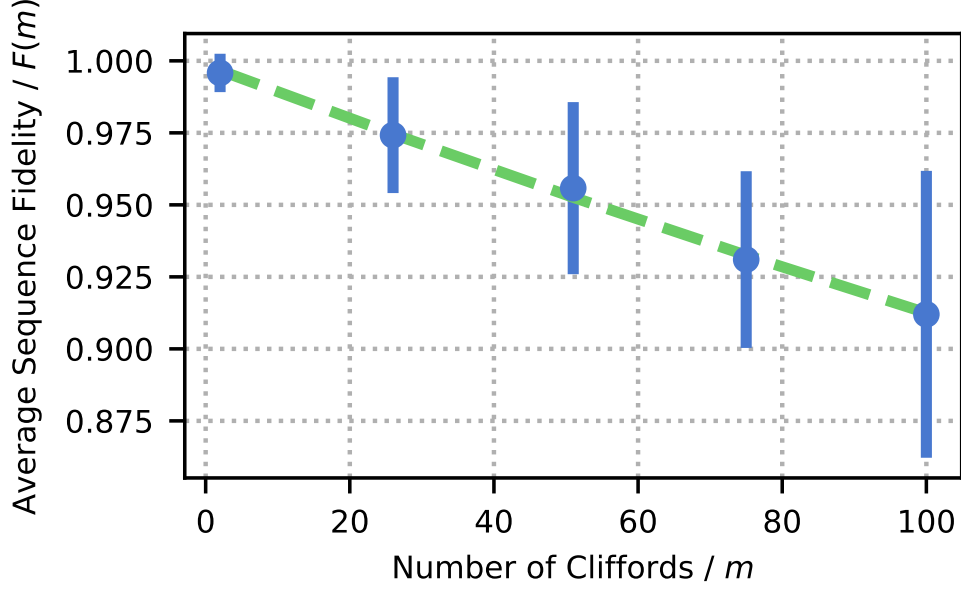


Figure 3.2: RBM fit

for readout are summarised in table ??, and a typical histogram of readout counts for one and two ions can be seen in figure ?. We find that the readout fidelity is XXX.

To measure the effect of state preparation and measurement error on longer experimental sequences, we will discuss randomised benchmarking in the following section 3.2.4. Due to the relevance here, we quote the measured state-preparation and measurement error (SPAM) of  $\epsilon_{SPAM} = 1.46(6) \times 10^{-3}$ .

### 3.2.4 Randomised Benchmarking

High fidelity unitary operations (gates) are essential for both near intermediate scale quantum computing and for reducing overheads in required physical qubits and operations in fault-tolerant schemes [?]. To evaluate the quality of both our state-prep and single qubit rotations, we employ randomized benchmarking (RBM) [?, ?]. RBM consists of applying random combinations of a pre-chosen discrete set of gates to estimate an average error per gate.



We chose the single-qubit Clifford group as our set of gates to evaluate. The single-qubit Clifford group is the set of unitaries which map the Pauli matrices to one another through conjugation. This can be thought of as the complete set of rotations of the Bloch sphere such that all valid combinations of the axis ( $x \rightarrow \{\pm x, \pm y, \pm z\}$ ), ( $y \rightarrow \{\pm x, \pm y, \pm z\}$ ), ( $z \rightarrow \{\pm x, \pm y, \pm z\}$ ) are realized. There are 24 unitaries in this set. We followed the RBM protocol described in the Thesis [?] to evaluate our single-qubit gates. First the qubit is prepared in some known initial state, i.e. prepared in some chosen basis. A gate sequence is then applied which consists of multiple random Clifford gates followed by a final ‘inverting’ Clifford, where the ‘inverting’ Clifford is chosen such that the full sequence performs the Identity operation. The state is then measured in the same basis to find any deviations from the Identity being performed due to gate errors. This is repeated with the same preparation and sequence multiple times to calculate the probability that the Identity was performed - thus giving the sequence fidelity. These steps are repeated for many different random sequences with a range of sequence lengths. The decay model we fit to the fidelity versus number of Clifford gates is given by,

$$F(m) = \frac{1}{2} (1 + (1 - 2\epsilon_{SPAM})(1 - 2\epsilon_c)^m), \quad (3.2)$$

where  $F(m)$  is the fidelity of the sequence of length  $m$ ,  $\epsilon_{SPAM}$  is the state-preparation and measurement error, and  $\epsilon_c$  is the average error per Clifford gate. We use this method to bench mark our qubit transition. The Clifford gates are decomposed into sequences of  $\pi/2$  and  $\pi$  pulses about either the  $x$ - or  $y$ -axes. We probe up to  $m = 100$  Clifford gates, and fit the decay of the fidelity to the above model. We measure the error per Clifford to be  $\epsilon_c = 9.5(3) \times 10^{-4}$ , while the SPAM error is  $\epsilon_{SPAM} = 1.46(6) \times 10^{-3}$ . The decay plot for this RBM sequence can be seen in figure ???. The error bars are given by the standard deviation of the survival populations. There are on average 3.50  $\pi/2$  pulses per Clifford, with a typical  $\pi/2$  duration of 1.3  $\mu$ s.

## 3.3 Motion

### 3.3.1 Cooling

For any interaction involving the motion of the ion, we require both the ability to prepare the motional state with high fidelity, and to subsequently measure this motional state to verify correct preparation. For entangling gates, and the creation of squeezed states which we are considering in this chapter, we assume that we begin in the motional ground state, or in other words, Fock state zero. Our initially trapped ions will be in some high temperature thermal state, (\*given by the oven temperature and the PI laser momenta kicks\*). We first doppler cool our ions, and then subsequently sideband cool them. We give a brief description of these two cooling processes here.

#### Doppler Cooling

Doppler cooling exploits the fact that incident light onto a moving ion will appear frequency shifted in the rest frame of the ion. For Doppler cooling of  $^{40}\text{Ca}^+$ , we apply both the 397 nm and 866 nm lasers. We initially red detune the 397 nm laser by around 100 MHz. This results in the preferential absorption of a quanta of 397 nm light by ions with a velocity vector antiparallel photon k-vector. After this absorption, the ion will be in the excited  $4P_{3/2}$  state and spontaneously decay to either the  $4S_{1/2}$ , or the  $3D_{3/2}$  emitting a photon of either 397 nm or of 866 nm respectively into a random direction. These two decay paths have a branching ratio of XX. As we desire many photon kicks to cool our ions, we repump the electron out of this metastable  $3D_{3/2}$  level by applying an on resonant 866 nm beam. The absorption and sequential emission of this 397 nm photon will lead to a net reduction in the motional energy of the ion if the photon is emitted at a higher energy than when absorbed. The equilibrium temperature is given by the condition where the doppler cooling rate is equal to photon recoil heating of the ion. Assuming a Lorentzian absorption profile, the minimum temperature is given by,

$$T_{\text{Doppler}} \approx \frac{\hbar\gamma}{2k_B}, \quad (3.3)$$

where  $\hbar$  is the reduced Planck constant,  $\gamma$  is the natural linewidth of the transition, and  $k_B$  is Boltzmann's constant.

For  $^{40}\text{Ca}^+$ , the natural linewidth of the 397 nm transition is  $\frac{\gamma}{2\pi} = 21$  MHz, leading to a Doppler temperature of approximately 0.5 mK. Given a radial mode frequency of  $\frac{\omega}{2\pi} = 4$  MHz, and the mean occupation number of the oscillator being given by,

$$\bar{n} = \frac{1}{e^{\hbar\omega/k_B T} - 1}, \quad (3.4)$$

we find the final thermal distribution to have an expected Fock state of  $\bar{n} = 2.3$ . Using parameters summarised in table ??, we find practically the final temperature after Doppler cooling to be around XXX mK.

### Sideband Cooling

To further cool the ions toward their motional ground state, we use resolved sideband cooling. The motion of the ion, described by a harmonic oscillator, modulates the transition frequencies of the ion, leading to sidebands at multiples of the motional frequency. For the  $4S_{1/2} \leftrightarrow 3D_{5/2}$  transition, at appropriate laser intensity and motional mode frequencies, these sidebands can be resolved spectroscopically. The pulsed sideband technique we employ consists of red sideband pulses, followed by deshelling, and repumping pulses on the 854 nm and 866 nm transitions respectively. An example pulse sequence can be seen in figure ??, and experimental parameters we use are summarised in table ??.

To verify the efficacy of our sideband cooling, we perform thermometry experiments by driving on resonance red sideband (RSB) and pi-RSB-pi pulse sequences. We record the time dynamics of population flopping as we vary RSB pulse length. In the case of Fock state zero, we expect to see a strong signal on the RSB, and no signal on the pi-RSB-pi pulses. We fit a thermal Fock state distribution (with truncation at Fock state = 100) to these signals to extract the mean occupation number, and  $\eta\Omega$ , the carrier Rabi frequency multiplied by the Lamb-Dicke parameter. A typical thermometry scan after Doppler and sideband cooling can be seen in figure ?. We find that the mean occupation number after sideband cooling is  $\bar{n} = 0.03()$ , and  $\eta\Omega = XX$  MHz.

Optimisation of the cooling parameters can be roughly performed by fitting temperature while scanning RSB pi-pulse durations, total number of pulses, repumping and deshelling times. One can optimise for minimum temperature, however it is also important to optimise for total cooling duration.

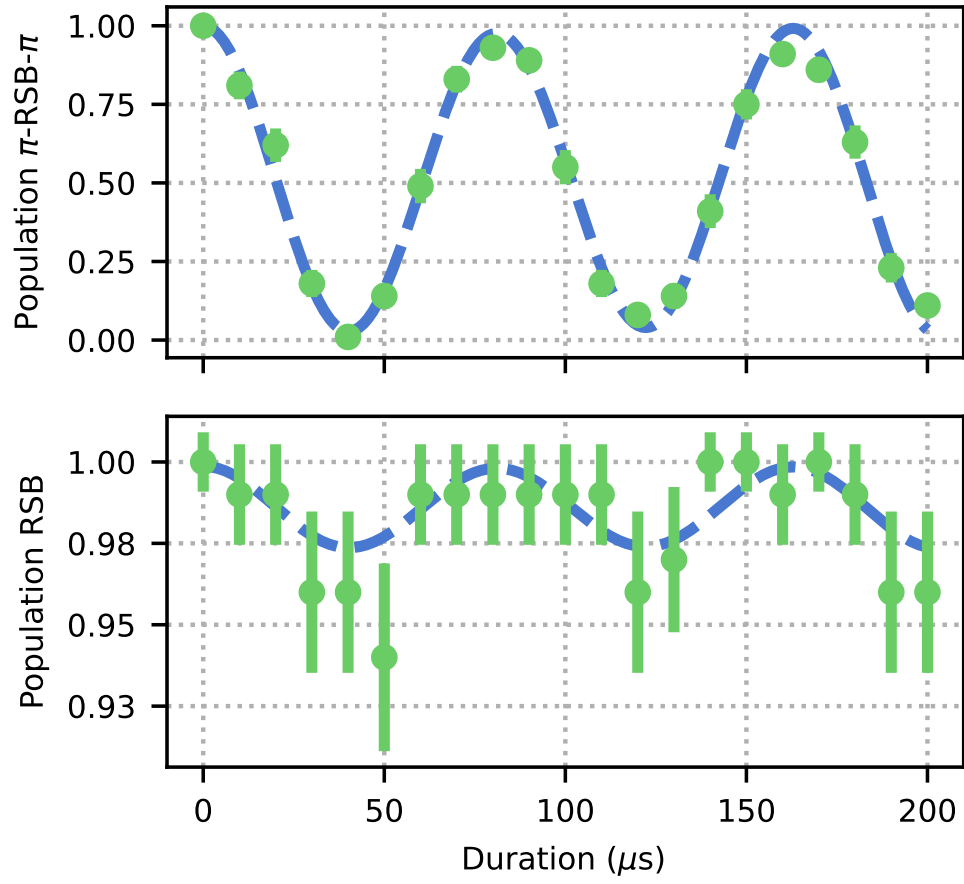


Figure 3.3: Thermometry after sideband cooling.

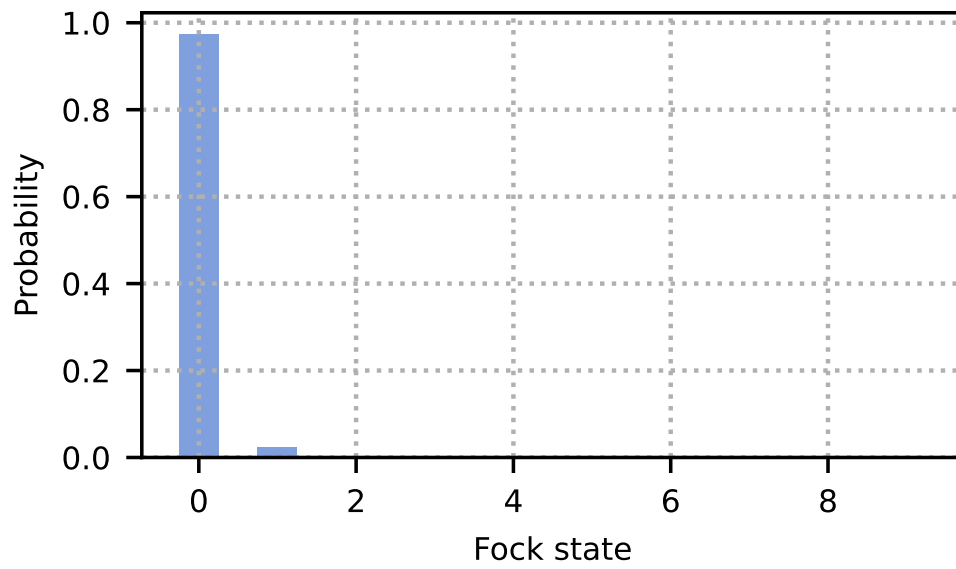


Figure 3.4: Fock state distribution

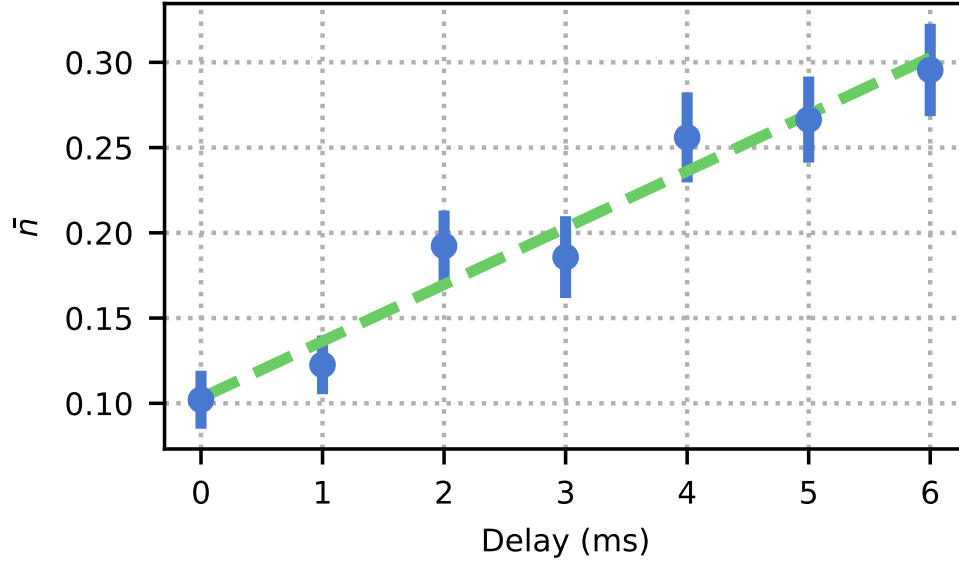


Figure 3.5: Heating rates of upper radial mode.

For single ion, single mode experiments, this duration is often a non-issue, however for multi-ion crystals, any interaction involving the motion, may require the sequential sideband cooling of multiple motional modes. This can not be easily parallalised due to the requirement that the RSB pi-pulse is performed near resonance to one of the motional sidebands. This sequential cooling strategy can be either limiting when heating and cooling rates are comparable, or in the best case, painful due to long data collection times. To mitigate this issue, other sub-Doppler cooling techniques with larger accepted frequency bandwidths may be employed. Examples are dark-resonance cooling[], and electromagnetically induced transparency (EIT) cooling[], and Sisyphus cooling[]. These techniques are not yet implemented in our system, but will be likely additions once we move to larger ion crystals.

### 3.3.2 Heating Rates

As mentioned, the cooling of our ions is only relevant if we have acceptable heating rates. Heating of the motion is predominantly caused by the ion trap itself. This can be due to imperfections in the surface of exposed dielectric and metals causing stray fields, or can be due to noise on the DC and RF drive voltages[]. Noise due to the surface of the trap can be mitigated by increasing ion-electrode distances, or by using traps with smaller surface area directly exposed to the ion. In our case, as mentioned in sections 2.2, the NPL trap has an electrode ion distance somewhat larger than most surface traps, but less than that of a macroscope blade or rod style trap. To verify the heating rate of our system, we performed a series of thermometry scans whilst varying some delay time between cooling and thermometry pulses. A typical plot can be seen in figure ???. We find that the heating rate of our system is approximately 33(3) quanta per second on the upper radial 4 MHz mode on one ion.

It is expected that the heating rate will be larger for lower frequency motional modes if we assume uniform electric field noise. We also verify this by looking at heating rate on the radial mode while varying the axial mode frequency. This is a useful diagnostic to check for unexpected heating at certain frequencies, perhaps due to RF noise in the lab. We find....

### 3.3.3 Motional Mode Stability

### 3.3.4 Motional Coherence Times

## 3.4 Spin-Dependent Forces

The spin-dependent force (SDF) is (planned to be) heavily used throughout this thesis. We use the Mølmer-Sørensen (MS) scheme [?], to generate the SDF via a bichromatic laser field. Bichromatic refers to the simultaneous application of two tones symmetrically detuned around the qubit carrier frequency, with absolute detuning approximately equal to the motional mode frequency,  $\delta \approx \omega_m$ . The resulting interaction, when ignoring off resonant and higher order couplings, is given by,

$$\hat{H}_{MS} = \hbar\eta\Omega \hat{\sigma}_\phi \cos(\delta t) \left( a e^{-i\omega_m t} + a^\dagger e^{i\omega_m t} \right), \quad (3.5)$$

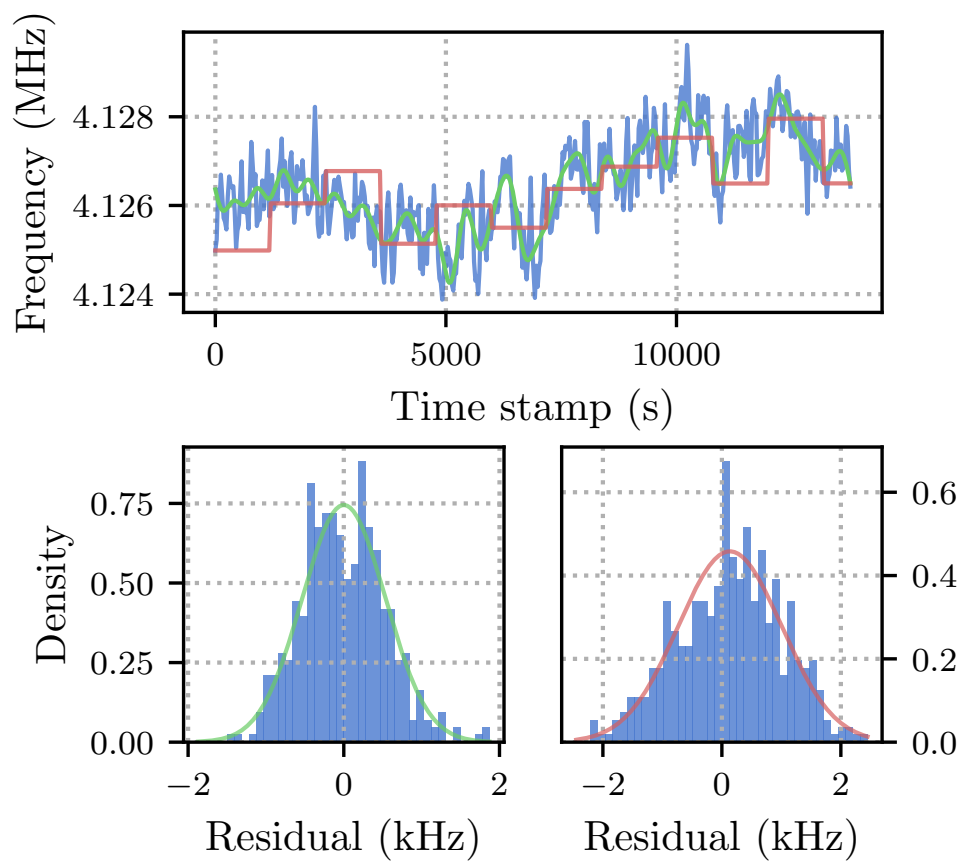


Figure 3.6: Motional mode frequency drift.



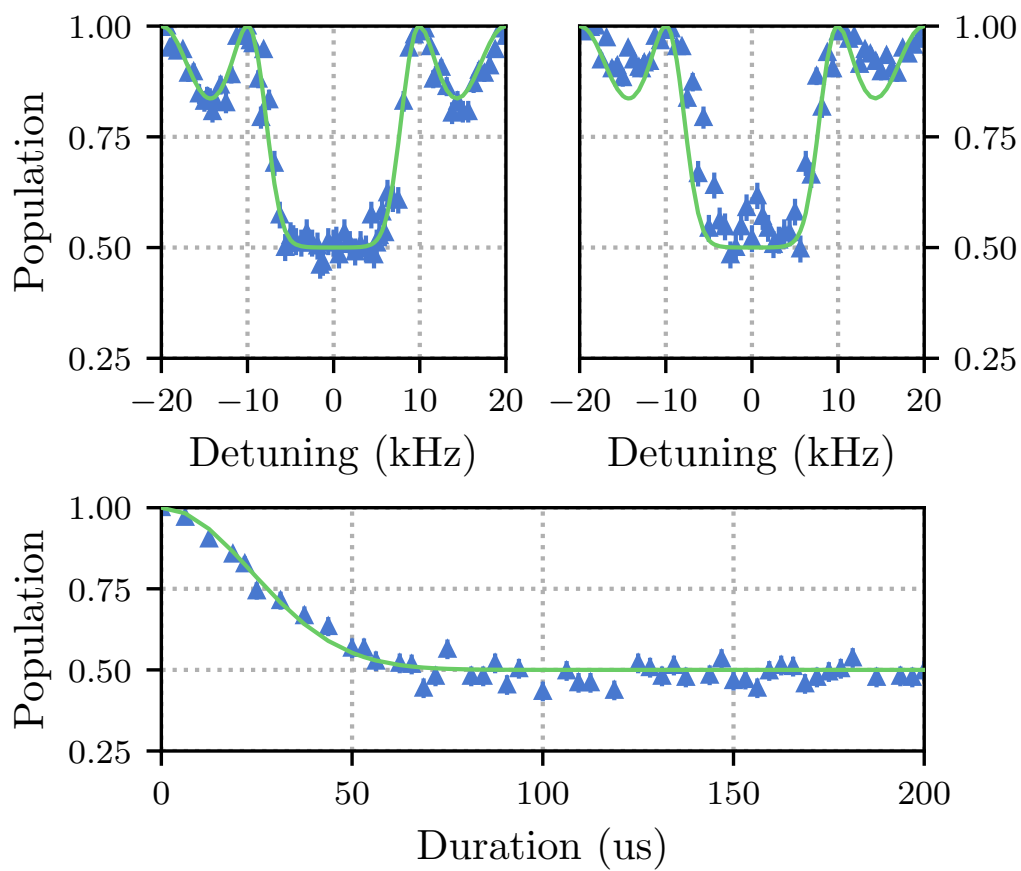


Figure 3.7: SDF traces.

where  $\eta$  is the Lamb-Dicke parameter,  $\Omega$  is the carrier Rabi frequency,  $a(a^\dagger)$  is the lowering (raising) operator, and  $\sigma_\phi$  is the Pauli operator with  $\phi$  being in the  $x, y$  -plane. Applying the rotating wave approximation, and defining  $\delta_g = \delta - \omega_m$ , we find that the interaction Hamiltonian can be approximated to,

$$\hat{H}_{MS} = \frac{\hbar\eta\Omega}{2} \hat{\sigma}_\phi \left( a e^{-i\delta_g t} + a^\dagger e^{i\delta_g t} \right). \quad (3.6)$$

The SDF realises a displacement of the motional state in phase space. We may control the trajectory of this displacement by varying  $\delta_g$ : on resonance,  $\delta_g = 0$ , we see linear trajectories, whilst off resonance,  $\delta_g \neq 0$ , we see cyclic trajectories where after some time  $t = 2\pi/\delta_g$ , the motion returns to the initial state. We shall exploit this control in both the two-qubit entangling gate experiments, as well as in the creation of squeezed states.

### 3.4.1 Calibrating the SDF

The MS interaction is widely used in ion trap experiments due to it being robust against varying initial motional states, and to the effects of heating during the pulse sequence. However, in our use case, the SDF is sensitive to miscalibration of the central qubit frequency, the balancing of power in the two tones, and to motional mode drifts. The first two miscalibrations appear as the SDF having.. We use both “detuning” and “duration” scans to calibrate the SDF. The “detuning” scan is performed by varying the detuning,  $\delta_{a_g}$ , of the interaction, whilst keeping the SDF duration constant, whilst the “duration” scan keeps detuning constant and varies the SDF duration. Duration scan fit given by,

$$P_{\downarrow, \text{th}} = \frac{1}{2} \left[ 1 + e^{-4(\bar{n} + \frac{1}{2})|\alpha(t)|^2} \right], \quad (3.7)$$

from Burd thesis, equation 3.30.  $|\alpha(t)| = \Omega_{sdf} t/2$ , fit find  $\Omega_{SDF} = 2\pi \times 6.6(2)$  kHz, fitted with  $\bar{n} = 0.03$  Fitting detuning scan using  $|\alpha(t)| = \Omega_{sdf} \sin(\delta t/2)/\delta$ , find  $\Omega_{SDF} = 2\pi \times 6.3(2)$  kHz, fitted with  $\bar{n} = 0.03$ .

## 3.5 Two-Qubit Entangling Gates

We perform two-qubit entangling gates using the Mølmer-Sørensen (MS) interaction [?]. This interaction is the same described SDF from the previous

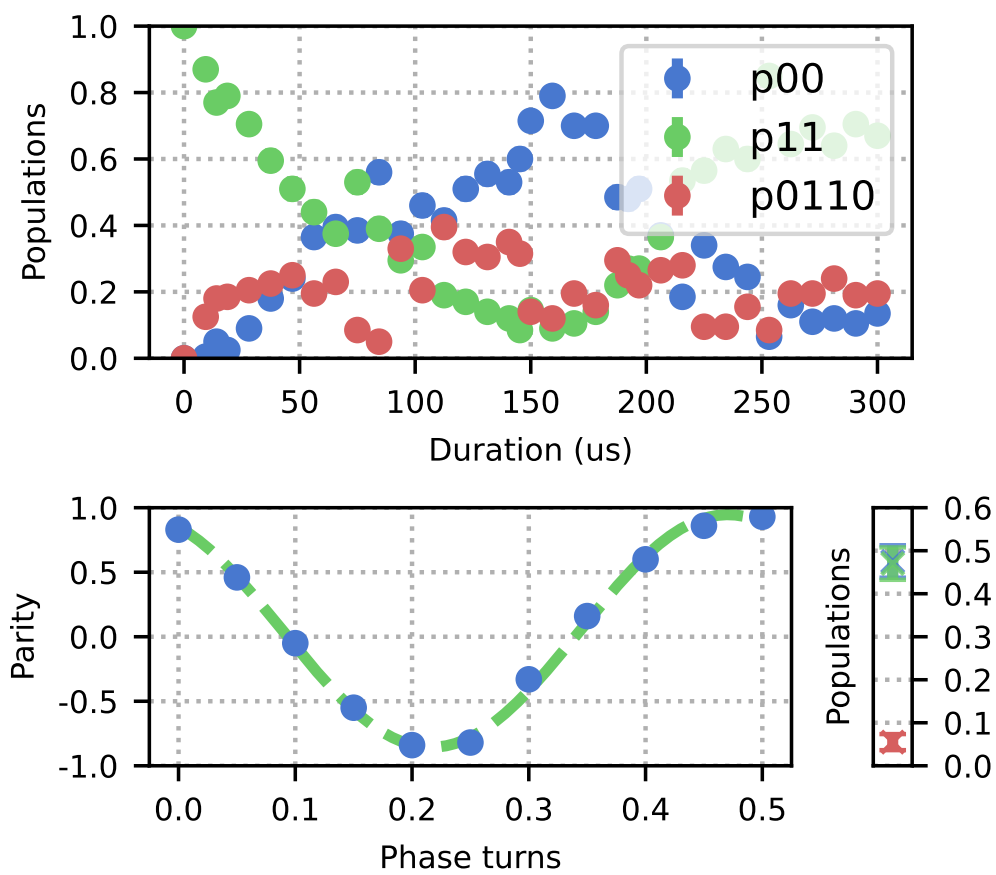


Figure 3.8: MS Gate.

section, but applied globally to two ions. The MS interaction relies on the spin dependent geometric phase accumulated during the motional displacement. To create a two-qubit entangled state, a differential geometric phase of  $\pi/2$  must be accumulated between the two-qubit basis states. To ensure there is no residual motional entanglement, the final motional state must return to the initial state. In practise, using an SDF detuned by  $\delta_g$ , this is achieved by applying the MS interaction for a time  $t = 2\pi/\delta_g$ . The MS gate is a universal two-qubit gate, and along with only single qubit gates, constitutes a universal gate set for discrete quantum algorithms.

Here we quote the fidelity of experimentally demonstrated two-qubit gates on our system. The fidelity serves to quantify the “closeness” or similarity of two density matrices. For the use case of quantum information processing, what we care about is that the experimental unitary applied in the gate sequence closely resembles the unitary we desire theoretically. In general this means that we should measure the fidelity of the applied unitary in an input state agnostic way. Unfortunately this is often not practical as the input state space can be unwieldy, and the act of preparing the input state can also be error prone. As a compromise we can apply the test unitary to either one, or to a set of input states, and measure the fidelity of the output state with respect to the known target state. If the error mechanisms of the test unitary are well understood, arguments can be made that this measured fidelity for a set of input state is representative (or not representative) of the average fidelity over the input state space.

Here for a two-qubit entangling gate, we target the creation of the Bell state  $|\Phi^+\rangle = 1/\sqrt{2}(|00\rangle + e^{i\phi_0}|11\rangle)$ , from an initial state of  $|11\rangle$ . The fidelity between our mixed state  $\rho$ , and the pure Bell state may be given by,

$$\mathcal{F} = \langle \Phi^+ | \rho | \Phi^+ \rangle = \frac{1}{2} (\rho_{00,00} + \rho_{11,11}) + \frac{1}{2} (e^{i\phi_0} \rho_{11,00} + e^{-i\phi_0} \rho_{00,11}), \quad (3.8)$$

To extract the fidelity experimentally we follow the popular protocol [?], where the first bracketted term of equation 3.8 is measured by performing projective measurements of the two ions after the gate sequence to extract populations, and the second bracketted term, known as the coherence terms, are measured by applying a global analysis  $\pi/2|_\phi$  pulse to the two ions and applying parity measurements. The contrast of the parity oscillations when varying the phase  $\phi$  of the  $\pi/2$  pulse yields the desired coherence term magnitude and phase. We require the creation of a Bell state for two qubit

entangling, however do not care what basis this state is in, and so float the target Bell state phase and take only the magnitude of the fitted parity oscillations for calculating the final fidelity.

The best two-qubit entangling gate fidelity currently achieved on our system is  $\mathcal{F} = 92(2)\%$ . As shown in figure 3.8, the magnitude of the parity scan was measured to be  $0.90(2)$ , while the populations  $(\rho_{00,00} + \rho_{11,11}) = 0.95(2)$ . Each population point in these figures are found by taking the average of 200 shots of the gate sequence.

These results serve as both a proof of principle for full spin control on our system, but also as a benchmark to which we can compare future system improvements. For future work, we will require the use of this entangling gate either as Bell state preparation for input to analogue simulation experiments [?], or as a primitive gate for the spin component of hybrid algorithms [?]. In both these cases, especially any use that requires multiple concatenated entangling gates, we will likely require improved gate fidelities. It is suspected that we are currently limited by nearby hot motional modes, and the lack of pulse ramping in our gate sequence. We expect that with the addition of pulse shaping we will be able to suppress the effect of nearby off-resonant transitions, and by sideband cooling of nearby motional modes we will further suppress contributions from unwanted spin-motion couplings.

## Chapter 4

## Outlook

## **4.1 Appendix**

### **4.1.1 Generating Ions**

### **4.1.2 Extracting Laser Offset and Magnetic Field**

## **4.2 Experimental Control**

## **4.3 Creating Squeezed States**